Atmos. Meas. Tech., 6, 1659–1671, 2013
www.atmos-meas-tech.net/6/1659/2013/
doi:10.5194/amt-6-1659-2013

Atmospheric Measurement Techniques
Open Access

Tracking isotopic signatures of CO_2 at the high altitude site Jungfraujoch with laser spectroscopy: analytical improvements and representative results

P. Sturm[1,*], B. Tuzson[1], S. Henne[1], and L. Emmenegger[1]

[1]Empa, Swiss Federal Laboratories for Materials Science and Technology, Laboratory for Air Pollution and Environmental Technology, Überlandstrasse 129, 8600 Dübendorf, Switzerland
[*]now at: Tofwerk AG, Uttigenstrasse 22, 3600 Thun, Switzerland

Correspondence to: B. Tuzson (bela.tuzson@empa.ch)

Received: 21 December 2012 – Published in Atmos. Meas. Tech. Discuss.: 15 January 2013
Revised: 5 June 2013 – Accepted: 10 June 2013 – Published: 12 July 2013

Abstract. We present the continuous data record of atmospheric CO_2 isotopes measured by laser absorption spectroscopy for an almost four year period at the High Altitude Research Station Jungfraujoch (3580 m a.s.l.), Switzerland. The mean annual cycles derived from data of December 2008 to September 2012 exhibit peak-to-peak amplitudes of 11.0 µmol mol^{-1} for CO_2, 0.60 ‰ for $\delta^{13}C$ and 0.81 ‰ for $\delta^{18}O$. The high temporal resolution of the measurements also allow us to capture variations on hourly and diurnal timescales. For CO_2 the mean diurnal peak-to-peak amplitude is about 1 µmol mol^{-1} in spring, autumn and winter and about 2 µmol mol^{-1} in summer. The mean diurnal variability in the isotope ratios is largest during the summer months too, with an amplitude of about 0.1 ‰ both in the $\delta^{13}C$ and $\delta^{18}O$, and a smaller or no discernible diurnal cycle during the other seasons. The day-to-day variability, however, is much larger and depends on the origin of the air masses arriving at Jungfraujoch. Backward Lagrangian particle dispersion model simulations revealed a close link between air composition and prevailing transport regimes and could be used to explain part of the observed variability in terms of transport history and influence region. A footprint clustering showed significantly different wintertime CO_2, $\delta^{13}C$ and $\delta^{18}O$ values depending on the origin and surface residence times of the air masses.

Several major updates on the instrument and the calibration procedures were performed in order to further improve the data quality. We describe the new measurement and calibration setup in detail and demonstrate the enhanced performance of the analyzer. A measurement precision of about 0.02 ‰ for both isotope ratios has been obtained for an averaging time of 10 min, while the accuracy was estimated to be 0.1 ‰, including the uncertainty of the calibration gases.

1 Introduction

Isotopes are ideal tracers of sources and sinks of carbon dioxide (CO_2). They provide unique information on the fluxes of CO_2 between the different pools involved in the carbon cycle. This is because the physical, chemical and biological exchange processes slightly fractionate between the different isotopes leading to characteristic isotopic signatures in the atmosphere, land and ocean. The carbon isotope composition of CO_2 ($\delta^{13}C$) is an excellent marker, for example, for partitioning oceanic and biospheric fluxes (Ciais et al., 1995; Keeling et al., 2011). Interpreting variations in the oxygen isotope composition of CO_2 ($\delta^{18}O$) is more challenging because the $\delta^{18}O$ is affected by both the carbon and water cycles (Farquhar et al., 1993). However, the $\delta^{18}O$ has been used to estimate gross biosphere fluxes (Ciais et al., 1997; Welp et al., 2011).

Stable isotope measurements traditionally rely on flask sampling and isotope ratio mass spectrometry (IRMS), reaching precisions for $\delta^{13}C$ and $\delta^{18}O$ in CO_2 of about 0.01 and 0.02 ‰, respectively (Werner et al., 2001). A novel alternative approach for measuring isotope ratios is laser spectroscopy. This optical technique allows for in situ measurements with high time resolution (up to 10 Hz), and

precisions up to 0.02 ‰ have been reached for $\delta^{13}C$ of atmospheric CO_2 (Richter et al., 2009). In addition to dedicated research instruments (Tuzson et al., 2008b; Richter et al., 2009), several commercial CO_2 isotope analyzers have become available in the last decade. A tunable diode laser absorption spectrometer using a liquid nitrogen cooled lead-salt laser enabled the study of isotopic carbon fluxes in terrestrial ecosystems (Bowling et al., 2003, 2005; Griffis et al., 2004, 2008). Other recent commercial instruments are based on cavity ring-down spectroscopy (Vogel et al., 2012), off-axis integrated cavity output spectroscopy (McAlexander et al., 2011), or quantum cascade laser absorption spectroscopy (Sturm et al., 2012). Another optical technique is based on Fourier transform infrared spectroscopy (Griffith et al., 2012).

Despite these analytical advancements, long-term measurements of tropospheric CO_2 isotopes using laser spectroscopy have not yet been reported. The goals for interlaboratory compatibility defined by the World Meteorological Organization (WMO) are 0.01 ‰ for $\delta^{13}C$ and 0.05 ‰ for $\delta^{18}O$ (WMO, 2011), which is very challenging independently of the technique used. Therefore, characterizing and improving the performance of CO_2 isotope analyzers is still essential, in particular when applied to monitoring of atmospheric background air.

Here we present our continuous data record of CO_2 isotopes measured by laser spectroscopy at the High Altitude Research Station Jungfraujoch, Switzerland, from December 2008 to September 2012. At this station, biweekly flask sampling and the analysis of the CO_2 isotopic composition by mass spectrometry started in 2000 (Sturm et al., 2005; van der Laan-Luijkx et al., 2012). Since December 2008, a state-of-the-art quantum cascade laser absorption spectrometer has also been deployed for continuous (1 Hz) in situ measurements of the isotopic composition of carbon dioxide (Tuzson et al., 2011). Based on the experiences gained from these measurements, several major updates on the instrument and the calibration procedures were performed in order to further improve the data quality. We describe our new measurement and calibration setup including the required data processing steps, show the performance of the improved analyzer and illustrate the capability of this method with representative results. Finally, backward Lagrangian particle dispersion simulations are used to distinguish the origin of the air masses arriving at Jungfraujoch and to establish a relationship between the potential source and sink regions and the observations.

2 Methods

2.1 Measurement site

The High Altitude Research Station Jungfraujoch (JFJ, 7°59′ E, 46°33′ N) is located on a mountain saddle on the northern ridge of the Swiss Alps at an altitude of 3580 m above sea level (Sphinx Observatory). The station is mostly situated in the free troposphere, but intermittently influenced by polluted planetary boundary layer (PBL) air reaching the site during synoptical uplifting or convection (Zellweger et al., 2003). The mean atmospheric pressure is 654 hPa and the mean annual temperature is −7.5 °C. Because of the high elevation, the year-round accessibility and the special geographical situation in the center of Europe the site is well suited for long-term monitoring of tropospheric background air but also for studying the transport of anthropogenic or biogenic tracers from the boundary layer to the free troposphere. A large number of trace gases and aerosol parameters are routinely monitored at Jungfraujoch as part of the Swiss National Air Pollution Monitoring Network (NABEL) and the Global Atmosphere Watch (GAW) programme of WMO.

2.2 Instrument setup

The quantum cascade laser absorption spectrometer employed for the CO_2 isotope monitoring was developed at Empa in collaboration with Aerodyne Research Inc. in 2007 and was presented in detail in Nelson et al. (2008) and Tuzson et al. (2008a). The instrument was first used for field studies near sources (Kammer et al., 2011; Tuzson et al., 2008a) and has been then deployed at Jungfraujoch (Tuzson et al., 2011). Briefly, the laser spectrometer uses a thermoelectrically cooled pulsed quantum cascade laser emitting at 4.3 µm. The instrument is based on differential absorption spectroscopy with two identical optical paths and a pair of multipass absorption cells with a path length of 7.3 m each to simultaneously analyze sample and reference gas. The laser emission frequency is scanned over the absorption lines of the three main CO_2 isotopologues $^{12}C^{16}O_2$, $^{13}C^{16}O_2$ and $^{18}O^{12}C^{16}O$ and the transmitted light is recorded with thermoelectrically cooled infrared detectors (PVI-3TE-4.4, Vigo Systems, Poland). A dedicated, commercially available software (TDLWintel, Aerodyne Research Inc., USA) is used for spectral analysis. The laser temperature and voltage, the cell temperature and pressure as well as the automatic calibrations including data processing into preliminary calibrated values are controlled using custom written LabVIEW code.

Sample air is drawn from the heated NABEL main inlet from the roof of the Sphinx laboratory. The sampling setup from December 2008 to November 2011 was as described in Tuzson et al. (2011) with a sample pump upstream of the instrument and four solenoid valves for calibration. This pump was removed in November 2011 as it had a small leak due to a damaged diaphragm, and from then on the sample air was drawn through the instrument by the pump downstream of the measurement cell only.

In this work we present analytical improvements and relevant new developments that we found necessary for long-term and reliable monitoring. In March 2012, i.e., after more than three years of spectroscopic measurement at the remote

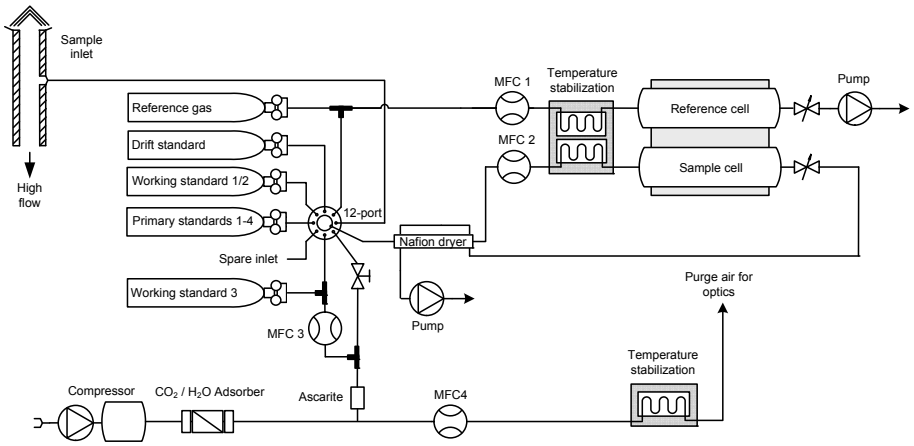

Fig. 1. Gas handling setup.

site Jungfraujoch, several hardware components were upgraded and a new calibration and gas-handling setup was implemented (Fig. 1). In the newly developed gas handling module, a 12-port multi-position valve (EMT2SD12MWE, VICI AG International, Switzerland) selects between the sample air stream and one of several primary and working standard gases. The sample cell flow rate is about $350\,\mathrm{mL\,min^{-1}}$. The reference cell is constantly flushed with compressed air from a cylinder at a flow rate of about $50\,\mathrm{mL\,min^{-1}}$. Both gas flows are temperature controlled and preheated to match the optical module temperature when entering into the multipass cells. The gas pressures in the reference and sample cell are measured by absolute pressure manometers and actively controlled at $80 \pm 0.003\,\mathrm{hPa}$ by adjusting the set points of two mass flow controllers (MFC2022, Axetris AG, Switzerland). Zero air is generated by an oil-free reciprocating air compressor and a carbon dioxide absorber/dryer (MCA1, Twin Tower Engineering, USA). Zero air is used to purge the optics housing at a flow rate of $1\,\mathrm{L\,min^{-1}}$ and occasionally to stepwise dilute a standard gas with a mass flow controller in order to correct for concentration dependence of the isotope ratios. The temperature stability of the optics was improved by adding further thermal insulation around the optical module and by using more precise PID (proportional-integral-derivative) temperature controllers (3216, Eurotherm Produkte AG, Switzerland). Thus, variations of the gas temperature in the measurement cells are typically damped by a factor of 100 compared to the laboratory air temperature variations (i.e., a 1 K change in the laboratory temperature results in a $\sim 10\,\mathrm{mK}$ change in the cell temperature). The stability of the cell temperature is typically about $\pm 5\,\mathrm{mK}$ over 24 h. Furthermore, the set point resolution of the laser temperature controller (LFI3751, Wavelength Electronics, USA) was enhanced by supplying an external voltage signal to the analogue input of the controller. This overcomes the limitations set by the digital-to-analog converter of the temperature controller and allows a much tighter control of the laser frequency and thus eliminates any spectral drift. Finally, the power supply of the laser driver was replaced by a low-noise device (PWS4323, Tektronix Inc., USA).

2.3 Calibration and data processing

The calibration procedure up to March 2012 was as described in Tuzson et al. (2011). Briefly, a drift standard was measured every 15 min, one calibration standard was measured every two hours and another calibration standard every 12 h. Each calibration gas was sampled for 300 s, except the drift standard, which was sampled for 128 s. Whenever any of the calibration standards was nearly empty, a new calibration cylinder with the same CO_2 concentration and isotopic composition was prepared and analyzed against the old standard cylinders, an in-house NOAA-ESRL standard (from NOAA Earth System Research Laboratory/Central Calibration Laboratory, USA, with the isotope composition analyzed by INSTAAR at the University of Colorado, USA) and occasionally against other calibrated standard gases. The CO_2 mole fraction of the calibration gases was measured by gas chromatography and since 2010 with a cavity ring-down spectrometer (G1301, Picarro Inc., USA) and linked to the WMO-X2007 scale using in-house NOAA-ESRL standards.

In spring 2012, an improved calibration strategy was implemented. A set of four primary standards was prepared (Table 1). Three standards were produced by mixing different amounts of CO_2 from different sources (marine carbonate; PanGas AG, Switzerland, and methane burning; Messer Schweiz AG, Switzerland) into aluminium cylinders and then diluted with synthetic air (79.5 % N_2, 20.5 % O_2). A fourth cylinder with a $\delta^{18}O$ value closer to the atmospheric $\delta^{18}O$ contains compressed air (Messer Schweiz AG, Switzerland). Subsamples of these gases were filled into 1.5 L glass flasks and the isotopic composition relative to the VPDB-CO_2 standard was determined by isotope ratio mass

Table 1. Primary standards with the assigned values on the WMO-X2007 scale for CO_2 and the VPDB-CO_2 scale for $\delta^{13}C$ and $\delta^{18}O$ as determined in spring 2012.

Tank no.	Mixture	CO_2 (µmol mol^{-1})	$\delta^{13}C$ (‰)	$\delta^{18}O$ (‰)
CB08984	CO_2 + syn. air	383.40	−3.54	−14.11
CB08970	CO_2 + syn. air	394.43	−8.00	−17.38
CB08999	CO_2 + syn. air	388.36	−12.01	−20.52
3076	compressed air	429.06	−10.57	−7.65

spectrometry in the WMO Central Calibration Laboratory at the Max-Planck-Institute for Biogeochemistry (MPI-BGC), Jena, Germany. The CO_2 mole fraction was linked to the WMO-X2007 scale by our NOAA-ESRL standards using the cavity ring-down spectrometer. The primary standards are expected to last for > 20 yr and our calibration scales are linked to these four gases. Three shorter-lived secondary working standards are then used to calibrate the instrument. These working standards are measured against the primary standards at Jungfraujoch about every two months to establish the working standard scale and to check for drifts in the working standard cylinders. They have a lifetime of about 1 yr and are replaced when the cylinder pressure decreases to below 30 bar. All calibration gases are stored in 30 L aluminium cylinders (Scott-Marrin, Inc., USA), except for one primary standard consisting of compressed air, which is a 20 L stainless steel cylinder. The reference and drift gases are contained in 50 L stainless steel cylinders. The regulators are two-stage high-purity brass regulators (412 Series, CONCOA, Pangas AG, Switzerland) and all tubing is either stainless steel tubing or Synflex tubing (SERTOflex 1300, Serto AG, Switzerland).

The new calibration procedure is as follows: every 30 min a drift cylinder (compressed air) is measured for 5 min. The three working standards are analyzed every 6 h for 5 min each. Two working standards are used to perform a two-point calibration for the CO_2 mole fraction and the isotope ratios. The third standard is treated as a target cylinder to check the stability of the working standard calibration. One working standard with a high CO_2 mole fraction is also used to measure every 5 days the concentration dependence of the isotopes by diluting it with zero air.

The isotopologue mole fractions based on spectral fitting require several data post-processing steps to obtain calibrated data. The processing procedure for the isotope ratios of the pre-March-2012 data consists of the following steps. First, a drift correction due to changes in gas temperature, laser frequency shifts, laser intensity fluctuations and gas pressure is applied. A multiple linear regression of the drift standard measurements with the four previously mentioned instrument parameters is performed to remove the influence of changing instrument parameters on the isotope ratios. The magnitude of this correction was typically 0–3 ‰, while the contribution of the influencing parameters varied from case to case. Since the relationship between the isotope ratios and one of the instrument parameters can change when there is a change in the system setup (i.e., new reference gas cylinder, stepwise adjustment of the laser frequency, change in the fitting parameters, etc.), raw data are analyzed in blocks with constant conditions. This lead to blocks of data spanning from a few days to a few weeks that were analyzed consecutively. A smoothing spline is applied to the residual variations still present in the corrected drift standard measurements and used to remove this remaining scatter from the sample and calibration measurements. The next step is the concentration dependence correction of the isotope ratios. Finally, the actual calibration is performed using one of the calibration standard measurements. For most of the 2009–2011 time period a one-point (offset) calibration is applied. The instrument response (slope of measured CO_2 versus WMO scale or measured isotope ratios versus VPDB-CO_2 scale, respectively) was determined from manual calibrations performed with different calibration gases and assumed to remain constant. This turned out to be the more robust calibration approach compared to using a 2-point calibration, because the uncertainty of the calculated calibration slope was larger than the real variations in the slope coefficients. Furthermore, data could also be calibrated in a consistent way at times when there was only one calibration gas available.

The improvements in the instrument stability implemented in spring 2012 allowed for a simplification of the data processing. In particular, the drift correction based on correlations with instrument parameters is obsolete. Instead, the drift standard measurements (every 30 min) are used in a first step to remove any drift. Next, the concentration dependence correction is applied. Third, the calibration coefficients (slope and offset) are calculated based on the 6-hourly calibration measurements. To further reduce the uncertainty in the calibration coefficients a smoothing spline is fitted to these values. The smoothed calibration coefficients are then applied to the sample data to get calibrated values. Finally, the 1 s data are averaged to 10 min mean values.

2.4 Transport simulations and footprint clustering

The Lagrangian particle dispersion model (LPDM) FLEXPART (Version 9.0) (Stohl et al., 2005) was used in backward mode to calculate source sensitivities for Jungfraujoch for the whole observation period. At each 3-hourly interval, 50 000 model particles were initialized at the location of Jungfraujoch and traced back in time for 10 days. FLEXPART considers horizontal and vertical displacements due to the mean atmospheric flow, turbulent mixing especially in the atmospheric boundary layer and vertical transport due to deep convection. Here, the model was driven by European Centre for Medium Range Weather Forecast (ECMWF)

operational analysis (00:00, 06:00, 12:00 and 18:00 UTC) and +3 h forecasts (03:00, 09:00, 15:00 and 21:00 UTC) with 91 vertical levels and a horizontal resolution of $0.2° \times 0.2°$ for the Alpine area (4° W–16° E, 39°–51° N) and $1° \times 1°$ for the global domain. The limited horizontal resolution of the model does not represent well the Alpine topography and, hence, a large difference between observatory and model altitude exists. In previous studies, the optimal release height for Jungfraujoch was determined to be at 3000 m above sea level, almost halfway between the real station's altitude and the model ground (Keller et al., 2011; Brunner et al., 2012). We adopted this initial altitude in the current study as well. The simulated source sensitivities can directly be multiplied with mass releases at a source grid cell, yielding simulated mole fractions at the receptor (Seibert and Frank, 2004). Source sensitivities are given in units s m^3 kg^{-1} and are also referred to as residence times or footprints. Source sensitivities were generated on a regular grid of $0.1° \times 0.1°$ covering Europe and a secondary grid of $0.5° \times 0.5°$ horizontal resolution for the Northern Hemisphere. The lowest vertical output level reached up to 100 m above model ground, which is the same as the minimal mixing height in the model.

In order to distinguish different transport regimes towards Jungfraujoch, source sensitivities were used in a clustering method. A straightforward clustering approach would be to treat the simulated source sensitivities in every grid cell as an individual variable in a cluster analysis. The number of cluster variables would then be equal to the number of grid cells in the output grid and quickly become too large to be efficiently handled by any cluster algorithm. Hence, a reduction of the cluster variables is required. This can be achieved by aggregating grid cells with small average residence times to larger grid cells, a procedure also used in regional scale inversion studies (Keller et al., 2011; Vollmer et al., 2009). Starting from grid cells with 0.1° resolution, we allowed aggregation to grid cells with up to 3.2° horizontal resolution, if the total residence time in the aggregated cells remained below a certain threshold. This threshold was iteratively deduced so that the total number of aggregated grid cells did not exceed 100. Only the European output domain was considered for the clustering, which will focus the separation of flow regimes more onto the regional scale transport and to a lesser degree onto inter-continental transport.

The clustering was performed on the time series of residence times of the aggregated surface grid cells only. Since these variables were not normally or log-normally distributed, we chose an alternative distance measure to obtain the dissimilarity matrix, **D** with elements $d_{i,j}$, that is used in the clustering process. Absolute distances between the ranks of the surface sensitivities over time were calculated according to

$$d_{i,j} = \sum_{k=1}^{N} \left| \mathrm{rank}(\tau_k)_i - \mathrm{rank}(\tau_k)_j \right|, \quad (1)$$

where the source sensitivities are indicated as τ and the index k runs over all aggregated grid cells N, while i and j refer to the time. The matrix **D** is symmetric and contains zeros in the diagonal. The off-diagonal elements contain the distance between two transport simulations at different times. Finally, based on the dissimilarity matrix the clustering was calculated using k-medoids clustering (Kaufman and Rousseeuw, 1990), which was previously successfully used for cluster analysis of single trajectory simulations (Henne et al., 2008). The number of selected clusters was obtained using the silhouette technique (Kaufman and Rousseeuw, 1990) by choosing the number of clusters (in the range 2 to 20) for which the average silhouette widths showed a local maximal. In the present case, a local maximum was obtained for 8 clusters with an average silhouette width of 0.16. A similar technique for clustering source sensitivities as obtained from LPDM calculations was presented by Hirdman et al. (2010). However, they aggregated residence times to larger regions defined by continental or country borders and Euclidean distances between these were used to derive the dissimilarity matrix.

To display the different flow regimes, average residence time maps per cluster were generated by summation over all cluster members and division by the number of clusters. For all clusters these show maximal values close to the site. In order to emphasize the differences between the individual clusters, the difference of cluster average and overall average residence times was computed and normalized by the mean of cluster and overall average (residence times by cluster normalized: RTCN). In this way, differences can be displayed in a linear and symmetric fashion, with RTCN values ranging from -2 to 2. Areas with RTCN larger than 0 indicate areas with greater than average surface contact and values larger than 1 indicate areas with 3 times larger residence times.

3 Results and discussion

3.1 Precision

The precision and stability of the updated instrument was characterized by the two-sample standard deviation (Werle et al., 1993) and is shown in Fig. 2. Tank air with a CO_2 mole fraction of 401 µmol mol^{-1} was continuously measured on site for 5 h. The two-sample standard deviation with 1 s data acquisition is compared with the initial performance measurements reported by Tuzson et al. (2008a). The most significant improvement compared to our previously reported values is the extended white-noise dominated region allowing for substantially longer averaging times ($\sim$ 10 times). The better operation stability reduces the requirements for frequent calibrations and thus minimizes the calibration gas consumption, which is of crucial importance for long-term monitoring. In addition, a lower instrumental drift is beneficial for the data post-processing, e.g., corrections and

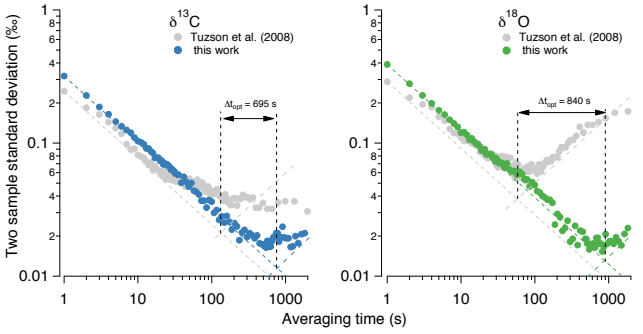

Fig. 2. Two-sample standard deviation (Allan deviation) of cylinder air measurements for $\delta^{13}C$ and $\delta^{18}O$. The stability performance of the upgraded instrument (colored markers) is compared with the values reported for this spectrometer by Tuzson et al. (2008a) (gray markers). The slight degradation in precision at 1 s averaging time is largely compensated by the higher stability at longer timescales (as indicated by Δt_{opt}). The optimum averaging time (t_{opt}) is reached after $\sim$ 12 min for both isotope ratios, corresponding to an analytical precision of 0.02 ‰. The white and drift noise influenced domains are indicated by gray and colored dashed lines.

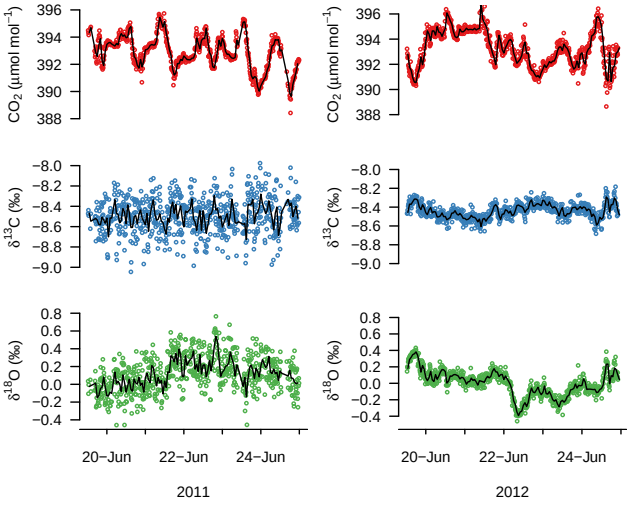

Fig. 3. Comparison of 10 min averaged data for six days in June 2011 and 2012, i.e., before and after the instrument upgrades. The solid lines are the 1 h averaged data.

calibrations. This stability improvement is a result of the better temperature, pressure and laser frequency control. As a consequence, the interval for the drift standard measurements was increased from 15 to 30 min. The precision of the CO_2 mole fraction measurement is 0.16 µmol mol^{-1} at 1 s and 0.01 µmol mol^{-1} at 10 min averaging time. The best precision of about 0.02 ‰ is reached for an averaging time of about 10 min for both isotope ratios.

The half hourly cylinder air measurements are still well correlated with the laboratory temperature (correlation coefficients of 0.6 to 0.8 for CO_2 and $\delta^{13}C$ and -0.4 to -0.7 for $\delta^{18}O$). Thus, temperature variations remain the major source for the drift on timescales longer than about 15 min, although it is not clear whether this is due to optical or electronic components that may both respond to temperature fluctuations.

A more detailed comparison of the precision before and after the instrument upgrades is shown in Fig. 3. It should be noted that the instrument has been running for more than two years almost unattended and without major revisions leading to some reduction in performance. During the selected time period of six days in June 2011 and June 2012 the CO_2 mole fraction was relatively constant between 390 and 396 µmol mol^{-1} and consequently the variations in the isotope ratios are small. The lower noise level in the 10 min averaged data for June 2012 is obvious and demonstrates the benefits of the instrument upgrades. Averaging to hourly mean values (solid lines in Fig. 3) greatly reduces the noise, in particular for the data before the upgrade. This is significant because data of background monitoring sites are usually reported as hourly mean values or even aggregated to longer intervals when compared with model output (e.g., from FLEXPART, see Sect. 3.4).

Four months of target cylinder measurements after the instrument upgrade are shown in Fig. 4. The assigned values of the target cylinders have been determined using the primary standards and the uncertainty ranges ($\pm 1\sigma$) are depicted as shaded areas in Fig. 4. Each single target cylinder measurement consists of a 120 s average and the standard deviation of the isotope ratio data of 0.06–0.07 ‰ roughly corresponds to the measurement precision at 120 s averaging time (Fig. 2). Analyzing the target cylinder for more than 120 s would most likely lead to an even smaller spread in the target cylinder data. However, there is a clear trade-off implemented in our sampling/calibration strategy. The target reference gas is measured for 5 min, but given the transition and flushing time of the spectrometer, the first 3 min are discarded and only the last 2 min are considered for analysis. Although the measurement precision in this case is by a factor 2.2 lower than the precision achievable using the optimum averaging time defined by the Allan variance minimum, it is still within the uncertainty of our primary standards (see Fig. 5). A slight reduction of the scatter in the target gas data (Fig. 4) would only be possible at the expense of significantly more target gas consumption (13 min vs. 5 min), which would involve their replacement every 5 instead of 12 months. We consider that the effort to produce, reference and transport these calibration gases as well as to assure continuity in the measurements outweighs the potential 0.02 ‰ improvement in precision.

Figure 5 shows the instrument response from the analysis of the four primary standards. The residuals of the linear fit between the measured and the assigned values indicate the linearity and accuracy of the instrument. The standard deviation of the residuals from Fig. 5 is 0.12 µmol mol^{-1} for CO_2, 0.06 ‰ for $\delta^{13}C$ and 0.13 ‰ for $\delta^{18}O$, respectively, which

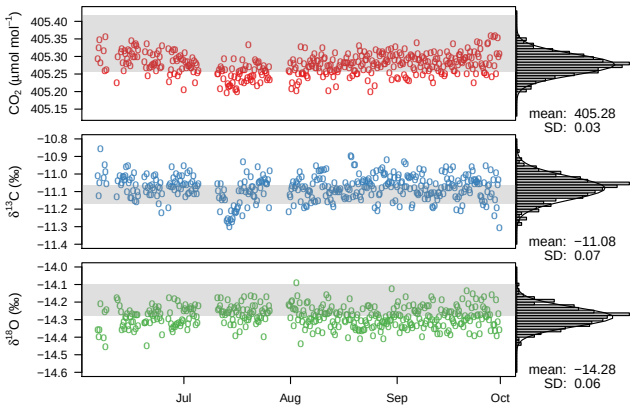

Fig. 4. Target gas measurements during four months (June to September 2012). The histograms show the distribution of the data with the respective mean and standard deviation. The shaded areas are the assigned values with the uncertainty (1σ) derived from the primary standard calibrations.

are typical values for the measurement of the four primary standards.

3.2 Long-term data record

An overview of the data record from December 2008 to September 2012 is shown in Fig. 6. Hourly averaged data for CO_2, $\delta^{13}C$ and $\delta^{18}O$ as well as fitted background curves are plotted. Two different methods have been used to calculate the long-term background values. The first method decomposes the signal into a long-term trend, a yearly cycle and short-term variations (Thoning et al., 1989). This curve fit consists of a combination of a polynomial (second order) and annual harmonic ($n = 4$) functions and the residuals from this fit are then smoothed using a low pass filter (80 days cutoff). The second method uses local regression (60 days window) to extract the baseline signal (Ruckstuhl et al., 2012). This is a non-parametric and thus very flexible approach and accounts for a possibly asymmetric contamination of the background signal (e.g., in winter local pollution always leads to a positive deviation from the background CO_2 concentration). The mean difference of the baseline values between the local regression and the smoothed curve fit are $-0.63 \pm 0.55\,\mu mol\,mol^{-1}$ for CO_2, 0.04 ± 0.04 ‰ for $\delta^{13}C$ and 0.06 ± 0.05 ‰ for $\delta^{18}O$, respectively. An ordinary least squares regression between the two baseline estimates yields slopes of 1.054 ($R^2 = 0.98$), 1.037 ($R^2 = 0.97$) and 1.024 ($R^2 = 0.98$) for CO_2, $\delta^{13}C$ and $\delta^{18}O$. Thus, both methods give very similar results and highlight the seasonal dynamics of the carbon dioxide and its isotopic composition in the atmosphere.

The gap in the time series in autumn 2011 was due to a pump failure. The diaphragm of the sample pump, which was originally installed upstream of the instrument, was broken. This resulted in a small leak and the influence of laboratory air could be seen as a small increase in the CO_2 mole fraction when people were present in the room. Data periods when the sample air was contaminated with laboratory air were removed based on a comparison with CO_2 data from another trace gas analyzer (G2401, Picarro Inc., USA), which uses the same air inlet. Data were flagged as contaminated by lab air, when the difference in the CO_2 mole fraction exceeded $2\,\mu mol\,mol^{-1}$. This is a conservative limit with regard to the isotope ratios, which were also affected by this contamination. Assuming that the CO_2 mole fraction in the well ventilated lab increases from 400 to $1000\,\mu mol\,mol^{-1}$ due to the presence of people in the laboratory and the $\delta^{13}C$ of the respired CO_2 is -23 ‰ (Epstein and Zeiri, 1988), one would expect a $\delta^{13}C$ of the laboratory air of about -17 ‰ (compared to -8 ‰ of the background CO_2). A contribution of $2\,\mu mol\,mol^{-1}$ CO_2 from laboratory air would then in turn lead to a change in the measured $\delta^{13}C$ of 0.045 ‰ at the most. This is less than the overall measurement uncertainty at that time. Using this procedure, 8 % of the data were removed during the period with the leak. Additionally, from 11 July to 16 September 2011 all data has been removed from further analysis because no CO_2 data from the trace gas analyzer was available during this period and as a result the data could not be screened for contamination.

We compared our laser based data with IRMS values from an intercomparison programme of $\delta^{13}C$ flask measurements (van der Laan-Luijkx et al., 2012). These samples were taken at Jungfraujoch between December 2007 and August 2011 and analyzed by three different IRMS laboratories. They revealed average differences between the laboratories of -0.02 to -0.03 ‰. The standard deviation of the individual differences was between 0.20 and 0.30 ‰. They conclude that the WMO goal for the measurement compatibility of $\delta^{13}C$ (± 0.01 ‰) (WMO, 2011) is not yet reached within this flask sampling program. If we compare our hourly averaged values that correspond to the flask sampling times with the flask results from the MPI-BGC laboratory then the average difference is -0.03 ‰ with a standard deviation of 0.19 ‰. This is similar to the differences between the flask samples and indicates that our data compare well with the flask data and within the inter-laboratory uncertainty of different isotope ratio mass spectrometry labs. For $\delta^{18}O$, the average difference to the MPI-BGC flask data is -0.31 ‰ with a standard deviation of 0.26 ‰ (W. Brand, personal communication, 2012). This substantial difference can be explained by the larger uncertainty in our $\delta^{18}O$ calibration scale, mainly because the $\delta^{18}O$ value of our standard gases (-24 to -10 ‰) did not span the range of the measured $\delta^{18}O$ values (~ 0 ‰). Flask data for comparison are not yet available for the period since March 2012, but we expect that both the precision and the accuracy have been improved by the instrument and calibration upgrades presented in this work. Nevertheless, continuing efforts are needed to evaluate the uncertainties and ensure the high accuracy and the traceability of the data, which are required at background monitoring sites like Jungfraujoch.

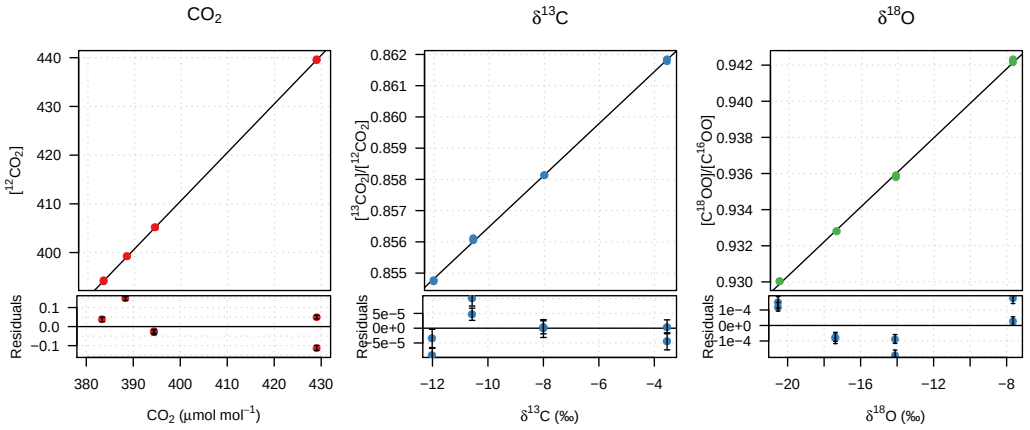

Fig. 5. Instrument response versus assigned values of the four primary standards as determined on 25 May 2012. The solid lines are weighted linear least squares fits to the data. The residuals from the fit are shown in the lower panels with the error bars representing the standard error of the mean. The ordinate represents the natural abundance weighted isotopologue ratios as retrieved by the spectrometer.

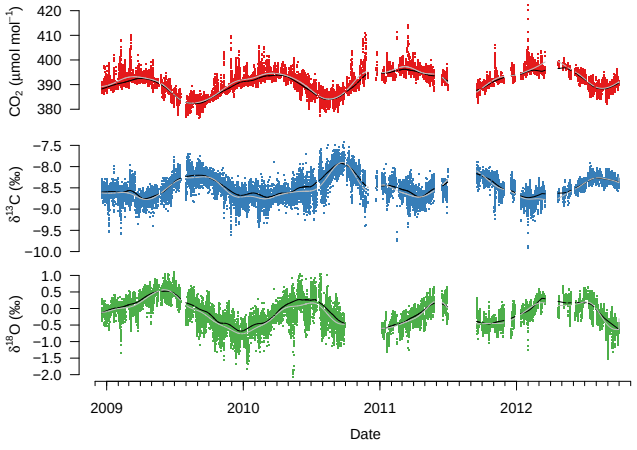

Fig. 6. Overview of the data record from December 2008 to September 2012. Hourly averaged data of CO_2 (red), $\delta^{13}C$ (blue) and $\delta^{18}O$ (green) as well as fitted background curves (black: local regression, gray: smooth curve fit, see text for explanation) are shown.

3.3 Mean seasonal and diurnal cycles

Mean annual cycles derived from the monthly bin-averaged data as well as from the annual harmonic part of the smooth curve fit are shown in Fig. 7. The averaged data have been detrended using the long-term trend derived from the smooth curve fit. The peak-to-peak amplitude of the seasonal variation is 11.0 µmol mol^{-1} for CO_2, 0.60 ‰ for $\delta^{13}C$ and 0.81 ‰ for $\delta^{18}O$. This is in good agreement with the seasonality obtained from independent flask measurements where amplitudes of 10.54 µmol mol^{-1} for CO_2 and 0.54 ‰ for $\delta^{13}C$ have been observed for the period between December 2007 and August 2011 (van der Laan-Luijkx et al., 2012).

The seasonality in CO_2 and $\delta^{13}C$ is dominated by the land biosphere and the relative contribution of photosynthesis and respiration (net ecosystem CO_2 exchange). The minimum in CO_2 mole fraction in August nearly coincides with the maximum in $\delta^{13}C$ and is due to peak net ecosystem CO_2 uptake. The CO_2 maximum and $\delta^{13}C$ minimum is reached around March when ecosystem respiration is dominating. In contrast to the seasonal cycle of CO_2 and $\delta^{13}C$, the seasonality of $\delta^{18}O$ is more complex. The $\delta^{18}O$ seasonal cycle is out of phase with CO_2 and $\delta^{13}C$ and shows its maximum in June and its minimum in December. This is a result of the interplay between the isotopic fluxes of photosynthesis and soil respiration (Peylin et al., 1999). Because of the isotopic equilibration with water, the $\delta^{18}O$ of CO_2 is strongly influenced by the oxygen isotopic composition of the leaf and soil water with which it is in contact. Therefore, the different seasonal phases of leaf discrimination, soil respiration and the oxygen isotope composition of precipitation are reflected in the seasonal cycle of atmospheric $\delta^{18}O$ (Yakir, 2003).

One distinct advantage of the high time-resolution measurements, compared to the traditional flask sampling, is that not only seasonal variations and long-term trends can be assessed, but also variations on hourly and diurnal timescales. This allows for combining the measurements with meteorology and therefore to interpret them in terms of atmospheric dynamics. The mean diurnal cycles of CO_2, $\delta^{13}C$ and $\delta^{18}O$ for the different seasons are shown in Fig. 8. Generally, the mean diurnal changes are small. For CO_2, the maximum occurs during the day with a peak-to-peak amplitude of about 1 µmol mol^{-1} in spring, autumn and winter. In summer, the mean amplitude is larger with the maximum at midday and a subsequent drop of the CO_2 mole fraction of about 2 µmol mol^{-1} in the afternoon, most likely due to uplift of boundary layer air, which is depleted in CO_2 because of photosynthetic uptake. These observations are in line with the PBL influence that was established for other parameters. The diurnal variations of aerosol parameters and other gaseous compounds measured at Jungfraujoch show almost no diurnal cycle in winter and a larger PBL influence in summer

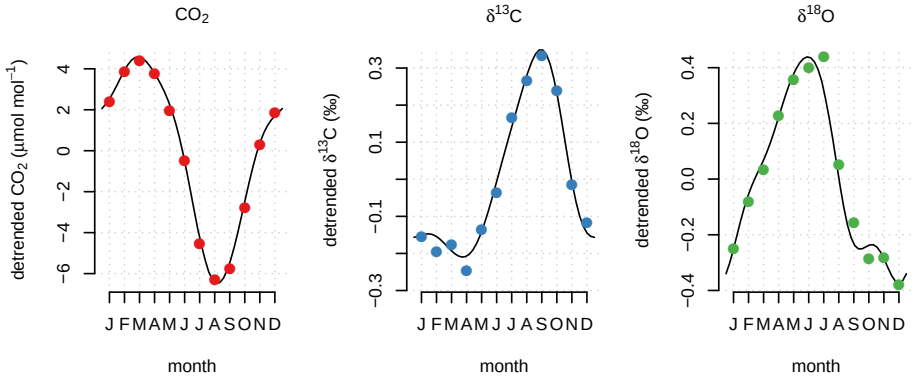

Fig. 7. Mean seasonal cycles from detrended and monthly bin-averaged data (points) and the annual harmonic part of the smoothed curve fit (lines). Error bars of the monthly averaged data are smaller than the plot symbols.

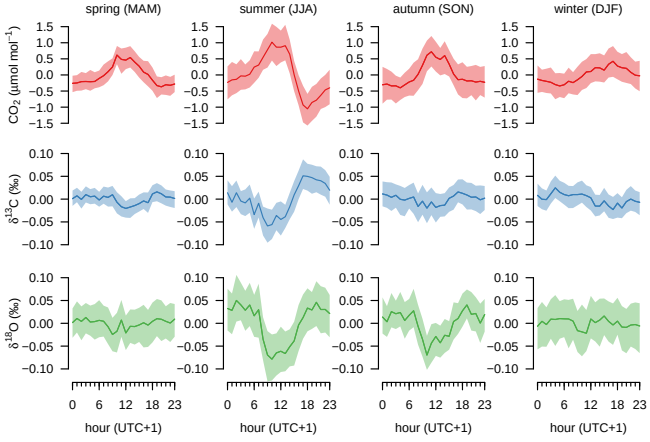

Fig. 8. Mean diurnal cycles as a difference to the daily mean for the different seasons. The shaded area is the 95 % confidence interval of the hourly mean derived from bootstrap resampling.

mostly due to thermally induced vertical transport (Zellweger et al., 2003; Collaud Coen et al., 2011). The diurnal variability is also seen in the isotope ratios with a maximum variation in the summer months of about 0.1 ‰ both in the $\delta^{13}C$ and $\delta^{18}O$, and a smaller or no discernible diurnal cycle during the other seasons.

3.4 Footprint clustering

The clustering algorithm described in Sect. 2.4 resulted in eight distinct clusters of air mass origins for Jungfraujoch and for the time period of January 2009 to April 2012. Figure 9 shows maps of the normalized residence time near the surface (footprint maps) obtained from the Lagrangian particle dispersion model FLEXPART. Clusters 1, 2 and 6 represent air masses with surface contact predominantly over south, east and north European land masses, respectively. Clusters 3 and 5 belong to flow regimes for which the surface sensitivities are extended to more distant and southeasterly and southwesterly directions, respectively. The clusters with the shortest residence time over ground are numbers 4, 3, 7 and 8. Cluster 4, in particular, seems to be representative of free tropospheric air without significant surface contact in Europe within the last 10 days before arriving at Jungfraujoch. Mainly North Atlantic influence can be attributed to cluster 7 and, with some additional contribution from the British Isles, to cluster 8.

To address the question whether the different transport regimes are reflected in our observations of CO_2 and its isotopic composition, we have aggregated the data into 3-hourly averages corresponding to the time steps of the model output. The data can then be grouped according to the eight different clusters (Fig. 10). The background concentrations derived from the local regression (Sect. 3.2) were subtracted from the CO_2, $\delta^{13}C$ and $\delta^{18}O$ values to obtain the short-term deviations from the background (ΔCO_2, $\Delta\delta^{13}C$ and $\Delta\delta^{18}O$). In order to minimize the influence of local transport processes (thermally induced transport), which are often not fully resolved in the transport model, only winter time data (December to February) were selected in Fig. 10. In winter, the Jungfraujoch is primarily situated in the free troposphere and is much less influenced by thermal convection of local boundary layer air as compared to the summer months (Zellweger et al., 2003). Including all data into this analysis would result qualitatively in the same picture with significant differences between clusters, although the differences are not as pronounced as for winter data only. The reason for this might be that apart from the thermally induced transport events also the spacial and temporal source and sink patterns are more complex in summer due the stronger biospheric activity.

The different concentrations and isotopic compositions between the clusters can be explained by the different residence times of the air within the surface layer and the different CO_2 emission rates and sources depending on the region. Figure 11 shows the median values per cluster as a function of the mean surface residence time. Generally, the longer the air masses stay within the lowest 100 m above ground, the

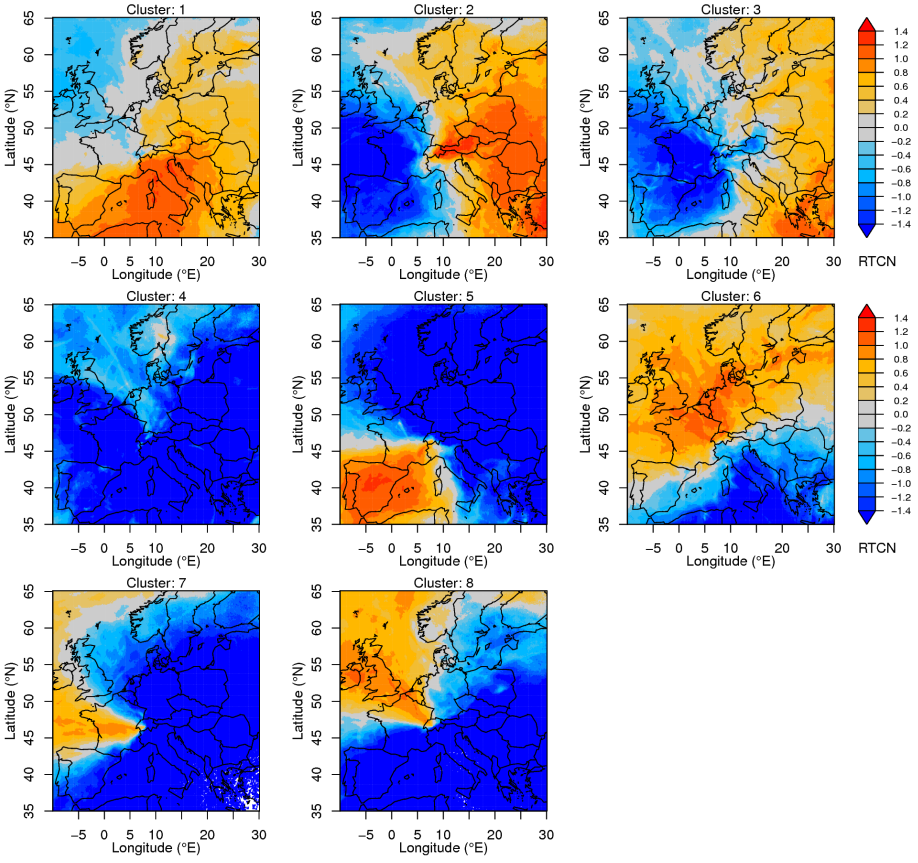

Fig. 9. Normalized residence time maps for different transport clusters for Jungfraujoch from January 2009 to April 2012 as obtained from FLEXPART simulations and footprint clustering. The color code indicates the cluster average source sensitivities at the surface relative to the overall footprint (RTCN: residence times by cluster normalized, see text for further explanation).

higher the CO_2 mole fraction and the lower the isotope ratios are. However, air parcels from clusters 2 and 6 have a smaller surface residence time by about 30 % compared to cluster 1, but rather higher concentrations. This indicates that emission rates are higher for clusters 2 and 6 than for cluster 1, which has the footprint area partially over the Mediterranean.

The two clusters with the most pronounced differences in the measured ΔCO_2 concentrations and isotope ratios are clusters 4 and 6. Cluster 4 has the lowest median ΔCO_2 value and correspondingly the highest values in $\Delta\delta^{13}C$ and $\Delta\delta^{18}O$. This agrees well with the footprint map showing no recent contribution from potentially polluted air masses. In contrast to cluster 4, cluster 6 has the highest ΔCO_2 concentrations, lowest $\Delta\delta^{18}O$ and second lowest $\Delta\delta^{13}C$ (after cluster 1). This can be explained by the relatively long surface residence time and the strong impact of air masses influenced by anthropogenic emissions from northwestern Europe including the high emission regions in the German Ruhr area and the Netherlands. The other clusters with high CO_2 concentrations are clusters 1 (Italy), 2 (eastern Europe) and partially 8 (UK), which agrees well with the high anthropogenic emissions expected from these influence regions. A pairwise comparison using the Wilcoxon rank sum test indicates that cluster 6 is significantly ($p < 0.001$) different from clusters 3, 4, 5 and 7 for ΔCO_2 and both isotope ratios. Cluster 4, in turn, is significantly ($p < 0.001$) different from clusters 1, 2, 6 and 8 for all three species. Thus, the CO_2, $\delta^{13}C$ and $\delta^{18}O$ signatures measured at Jungfraujoch distinctly vary according to the different transport patterns.

4 Conclusions

We present a high time-resolution record of the isotopic carbon dioxide composition in the atmosphere measured at the background monitoring site Jungfraujoch from December 2008 to September 2012 by laser absorption spectroscopy. In spring 2012, the data quality has been further improved by minimizing instrumental drift and by optimizing the calibration setup.

The mean annual cycles derived from almost four years of data revealed peak-to-peak amplitudes of 11.0 µmol mol^{-1} for CO_2, 0.60 ‰ for $\delta^{13}C$ and 0.81 ‰ for $\delta^{18}O$. A major benefit of the high time-resolution measurements compared to the traditional flask sampling is that, in addition to seasonal

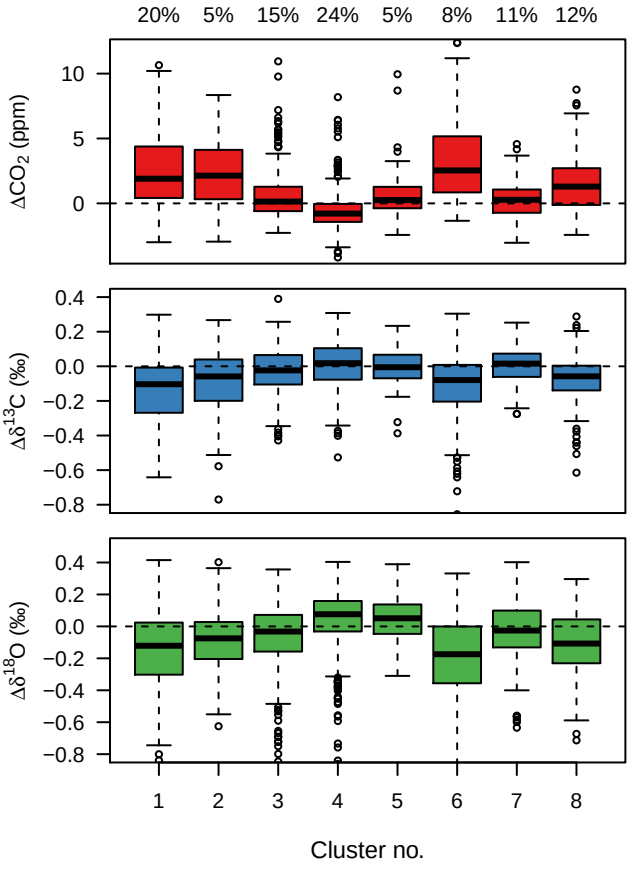

Fig. 10. Boxplots of CO_2, $\delta^{13}C$ and $\delta^{18}O$ deviations from the background concentrations (Δ) for the winter months (December to February) classified by the different footprint clusters. The boxes show the interquartile range and the whiskers extend to the most extreme data point, which is no more than 1.5 times the interquartile range away from the box. The percentages at the top indicate the cluster frequencies.

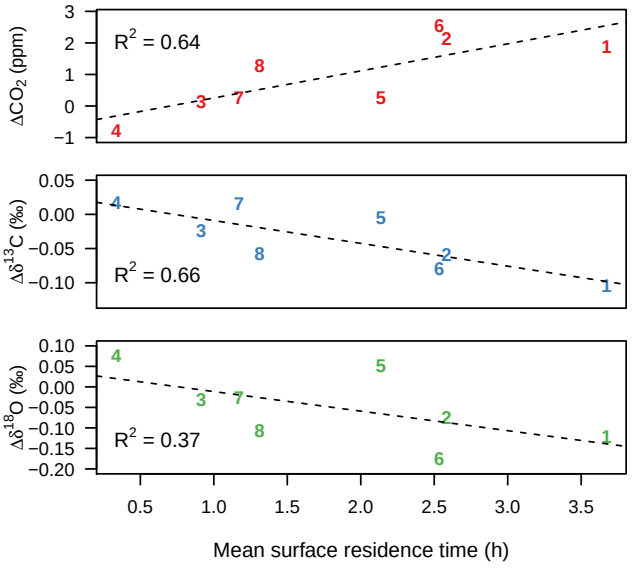

Fig. 11. Median ΔCO_2, $\Delta\delta^{13}C$ and $\Delta\delta^{18}O$ of the eight footprint clusters as a function of the mean residence time within a layer of 100 m above ground for the winter months (December to February). The colored numbers indicate the cluster index and the dashed lines are the ordinary least squares regression lines.

variations and long-term trends, also variations on hourly and diurnal timescales can be captured. This allows to reliably estimate representative background values of CO_2 and its isotope ratios. On hourly and diurnal timescales there is considerable variation since the site is intermittently influenced by free tropospheric and atmospheric boundary layer air masses. Only sufficiently high time resolution allows relating the observations to high-resolution transport models, regional-scale ecosystem models, and regional-scale flux inversions.

The mean diurnal cycles of CO_2 and its isotopic composition are small at Jungfraujoch. For CO_2, the mean diurnal peak-to-peak amplitude is about 1 µmol mol^{-1} in spring, autumn and winter, and about 2 µmol mol^{-1} in summer. The mean diurnal variability in the isotope ratios shows a maximum of about 0.1 ‰ both in the $\delta^{13}C$ and $\delta^{18}O$ in the summer months, and a smaller or no discernible diurnal cycle during the other seasons. The day-to-day variability, however, can be much larger depending on the origin of the air masses arriving at Jungfraujoch. Backward Lagrangian particle dispersion model simulations revealed a close link between air composition and prevailing transport regimes and were able to explain part of the observed variability in terms of transport history and influence region. The footprint clustering, which was applied to the model output, showed significantly different wintertime CO_2, $\delta^{13}C$ and $\delta^{18}O$ values depending on the air mass origin and surface residence times.

Long-term, high-resolution measurements of CO_2 isotopes and tracing the observed variabilities back to their origin will improve the understanding of the carbon cycle. For example, estimates of global photosynthesis based on atmospheric $\delta^{18}O$ rely on estimates of the CO_2 hydration efficiency, i.e., the percentage of CO_2 molecules entering a leaf or the soil that isotopically equilibrate with plant and soil water. This CO_2 hydration efficiency is still a substantial source of uncertainty (Wingate et al., 2009; Welp et al., 2011) and high time-resolution data records such as the time series presented here, combined with an atmospheric transport model and a terrestrial biosphere model of $\delta^{18}O$ (Cuntz et al., 2003) will be valuable for further constraining such estimates.

As the CO_2 isotope measurements are continuing and because of the increased data quality, we expect to be able to analyze distinct events and tracer relationships depending on weather conditions and attribute these to specific emission/uptake locations and processes. Other related tracers, e.g., $\delta(O_2/N_2)$ (Uglietti et al., 2011), carbon monoxide (Dils et al., 2011), and carbonyl sulfide that are routinely measured at Jungfraujoch, can provide additional information on the sources and sinks of CO_2. Combining these data with an

isotope specific regional model might allow for emission specific classifications. In this context, radiocarbon (^{14}C) observations can also be used to separate biospheric fluxes from fossil fuel CO_2 emissions (Levin et al., 2003). Up to now, $^{14}CO_2$ measurements were too costly to be performed on hourly timescales. However, with further advances in laser spectroscopy, continuous high-resolution $^{14}CO_2$ measurements might become feasible in the future (Galli et al., 2011). This would allow a direct determination of fossil fuel derived CO_2 and complement the information that can be obtained with continuous stable isotope measurements.

Acknowledgements. We thank the International Foundation High Altitude Research Stations Jungfraujoch and Gornergrat (HFSJG) for access to the facilities at the Research Station Jungfraujoch and the custodians for on-site support. We also thank W. Brand (Max-Planck-Institute for Biogeochemistry, Jena, Germany) for linking our primary standard gases to the VPDB scale and providing the flask $\delta^{18}O$ data. This project was funded by the Swiss National Science Foundation and the Swiss Federal Office for the Environment.

Edited by: P. Werle

References

Bowling, D., Sargent, S., Tanner, B., and Ehleringer, J.: Tunable diode laser absorption spectroscopy for stable isotope studies of ecosystem–atmosphere CO_2 exchange, Agr. Forest Meteorol., 118, 1–19, doi:10.1016/S0168-1923(03)00074-1, 2003.

Bowling, D., Burns, S., Conway, T., Monson, R., and White, J.: Extensive observations of CO_2 carbon isotope content in and above a high-elevation subalpine forest, Global Biogeochem. Cy., 19, GB3023, doi:10.1029/2004GB002394, 2005.

Brunner, D., Henne, S., Keller, C. A., Reimann, S., Vollmer, M. K., O'Doherty, S., and Maione, M.: An extended Kalman-filter for regional scale inverse emission estimation, Atmos. Chem. Phys., 12, 3455–3478, doi:10.5194/acp-12-3455-2012, 2012.

Ciais, P., Tans, P., White, J., Trolier, M., Francey, R., Berry, J., Randall, D., Sellers, P., Collatz, J., and Schimel, D.: Partitioning of ocean and land uptake of CO_2 as inferred by $\delta^{13}C$ measurements from the NOAA Climate Monitoring and Diagnostics Laboratory Global Air Sampling Network, J. Geophys. Res., 100, 5051–5070, 1995.

Ciais, P., Denning, A., Tans, P., Berry, J., Randall, D., Collatz, G., Sellers, P., White, J., Trolier, M., Meijer, H., Francey, R., Monfray, P., and Heimann, M.: A three-dimensional synthesis study of $\delta^{18}O$ in atmospheric CO_2. 1. Surface Fluxes, J. Geophys. Res.-Atmos., 102, 5857–5872, 1997.

Collaud Coen, M., Weingartner, E., Furger, M., Nyeki, S., Prévôt, A. S. H., Steinbacher, M., and Baltensperger, U.: Aerosol climatology and planetary boundary influence at the Jungfraujoch analyzed by synoptic weather types, Atmos. Chem. Phys., 11, 5931–5944, doi:10.5194/acp-11-5931-2011, 2011.

Cuntz, M., Ciais, P., Hoffmann, G., Allison, C., Francey, R., Knorr, W., Tans, P., White, J., and Levin, I.: A comprehensive global three dimensional model of $\delta^{18}O$ in atmospheric CO_2: 2. Mapping the atmospheric signal, J. Geophys. Res, 108, 4528, doi:10.1029/2002JD003153, 2003.

Dils, B., Cui, J., Henne, S., Mahieu, E., Steinbacher, M., and De Mazière, M.: 1997–2007 CO trend at the high Alpine site Jungfraujoch: a comparison between NDIR surface in situ and FTIR remote sensing observations, Atmos. Chem. Phys., 11, 6735–6748, doi:10.5194/acp-11-6735-2011, 2011.

Epstein, S. and Zeiri, L.: Oxygen and carbon isotopic compositions of gases respired by humans, P. Natl. Acad. Sci., 85, 1727–1731, 1988.

Farquhar, G. D., Lloyd, J., Taylor, J. A., Flanagnan, L. B., Syvertsen, J. P., Hubick, K. T., Wong, S. C., and Ehleringer, J. R.: Vegetation effects on the isotope composition of oxygen in atmospheric CO_2, Nature, 363, 439–443, 1993.

Galli, I., Bartalini, S., Borri, S., Cancio, P., Mazzotti, D., De Natale, P., and Giusfredi, G.: Molecular Gas Sensing Below Parts Per Trillion: Radiocarbon-Dioxide Optical Detection, Phys. Rev. Lett., 107, 270802, doi:10.1103/PhysRevLett.107.270802, 2011.

Griffis, T., Baker, J., Sargent, S., Tanner, B., and Zhang, J.: Measuring field-scale isotopic CO_2 fluxes with tunable diode laser absorption spectroscopy and micrometeorological techniques, Agr. Forest Meteorol., 124, 15–29, doi:10.1016/j.agrformet.2004.01.009, 2004.

Griffis, T., Sargent, S., Baker, J., Lee, X., Tanner, B., Greene, J., Swiatek, E., and Billmark, K.: Direct measurement of biosphere-atmosphere isotopic CO_2 exchange using the eddy covariance technique, J. Geophys. Res., 113, D08304, doi:10.1029/2007JD009297, 2008.

Griffith, D. W. T., Deutscher, N. M., Caldow, C., Kettlewell, G., Riggenbach, M., and Hammer, S.: A Fourier transform infrared trace gas and isotope analyser for atmospheric applications, Atmos. Meas. Tech., 5, 2481–2498, doi:10.5194/amt-5-2481-2012, 2012.

Henne, S., Klausen, J., Junkermann, W., Kariuki, J. M., Aseyo, J. O., and Buchmann, B.: Representativeness and climatology of carbon monoxide and ozone at the global GAW station Mt. Kenya in equatorial Africa, Atmos. Chem. Phys., 8, 3119–3139, doi:10.5194/acp-8-3119-2008, 2008.

Hirdman, D., Sodemann, H., Eckhardt, S., Burkhart, J. F., Jefferson, A., Mefford, T., Quinn, P. K., Sharma, S., Ström, J., and Stohl, A.: Source identification of short-lived air pollutants in the Arctic using statistical analysis of measurement data and particle dispersion model output, Atmos. Chem. Phys., 10, 669–693, doi:10.5194/acp-10-669-2010, 2010.

Kammer, A., Tuzson, B., Emmenegger, L., Knohl, A., Mohn, J., and Hagedorn, F.: Application of a quantum cascade laser-based spectrometer in a closed chamber system for real-time $\delta^{13}C$ and $\delta^{18}O$ measurements of soil-respired CO_2, Agr. Forest Meteorol., 151, 39–48, doi:10.1016/j.agrformet.2010.09.001, 2011.

Kaufman, L. and Rousseeuw, P.: Finding Groups in Data. An Introduction to Cluster Analysis, John Wiley and Sons, New York, 1990.

Keeling, C. D., Piper, S. C., Whorf, T. P., and Keeling, R. F.: Evolution of natural and anthropogenic fluxes of atmospheric CO_2 from 1957 to 2003, Tellus B, 63, 1–22, doi:10.1111/j.1600-0889.2010.00507.x, 2011.

Keller, C., Brunner, D., Henne, S., Vollmer, M., O'Doherty, S., and Reimann, S.: Evidence for under-reported western European emissions of the potent greenhouse gas HFC-23, Geophys. Res.

Lett., 38, L15808, doi:10.1029/2011GL047976, 2011.

Levin, I., Kromer, B., Schmidt, M., and Sartorius, H.: A novel approach for independent budgeting of fossil fuel CO_2 over Europe by $^{14}CO_2$ observations, Geophys. Res. Lett., 30, 2194, doi:10.1029/2003GL018477, 2003.

McAlexander, I., Rau, G., Liem, J., Owano, T., Fellers, R., Baer, D., and Gupta, M.: Deployment of a carbon isotope ratiometer for the monitoring of CO_2 sequestration leakage, Anal. Chem., 83, 6223–6229, doi:10.1021/ac2007834, 2011.

Nelson, D., McManus, J., Herndon, S., Zahniser, M., Tuzson, B., and Emmenegger, L.: New method for isotopic ratio measurements of atmospheric carbon dioxide using a 4.3 µm pulsed quantum cascade laser, Appl. Phys. B-Lasers O., 90, 301–309, doi:10.1007/s00340-007-2894-1, 2008.

Peylin, P., Ciais, P., Denning, A. S., Tans, P. P., Berry, J. A., and White, J. W. C.: A 3-dimensional study of $\delta^{18}O$ in atmospheric CO_2: contribution of different land ecosystems, Tellus B, 51, 642–667, doi:10.1034/j.1600-0889.1999.t01-2-00006.x, 1999.

Richter, D., Wert, B. P., Fried, A., Weibring, P., Walega, J. G., White, J. W. C., Vaughn, B. H., and Tittel, F. K.: High-precision CO_2 isotopologue spectrometer with a difference-frequency-generation laser source, Opt. Lett., 34, 172–174, 2009.

Ruckstuhl, A. F., Henne, S., Reimann, S., Steinbacher, M., Vollmer, M. K., O'Doherty, S., Buchmann, B., and Hueglin, C.: Robust extraction of baseline signal of atmospheric trace species using local regression, Atmos. Meas. Tech., 5, 2613–2624, doi:10.5194/amt-5-2613-2012, 2012.

Seibert, P. and Frank, A.: Source-receptor matrix calculation with a Lagrangian particle dispersion model in backward mode, Atmos. Chem. Phys., 4, 51–63, doi:10.5194/acp-4-51-2004, 2004.

Stohl, A., Forster, C., Frank, A., Seibert, P., and Wotawa, G.: Technical note: The Lagrangian particle dispersion model FLEXPART version 6.2, Atmos. Chem. Phys., 5, 2461–2474, doi:10.5194/acp-5-2461-2005, 2005.

Sturm, P., Leuenberger, M., and Schmidt, M.: Atmospheric O_2, CO_2 and $\delta^{13}C$ observations from the remote sites Jungfraujoch, Switzerland, and Puy de Dome, France, Geophys. Res. Lett., 32, L17811, doi:10.1029/2005GL023304, 2005.

Sturm, P., Eugster, W., and Knohl, A.: Eddy covariance measurements of CO_2 isotopologues with a quantum cascade laser absorption spectrometer, Agr. Forest Meteorol., 152, 73–82, doi:10.1016/j.agrformet.2011.09.007, 2012.

Thoning, K., Tans, P., and Komhyr, W.: Atmospheric carbon dioxide at Mauna Loa Observatory: 2. Analysis of the NOAA GMCC data, 1974–1985, J. Geophys. Res., 94, 8549–8565, 1989.

Tuzson, B., Mohn, J., Zeeman, M., Werner, R., Eugster, W., Zahniser, M., Nelson, D., McManus, J., and Emmenegger, L.: High precision and continuous field measurements of $\delta^{13}C$ and $\delta^{18}O$ in carbon dioxide with a cryogen-free QCLAS, Appl. Phys. B-Lasers O., 92, 451–458, doi:10.1007/s00340-008-3085-4, 2008a.

Tuzson, B., Zeeman, M., Zahniser, M., and Emmenegger, L.: Quantum cascade laser based spectrometer for in situ stable carbon dioxide isotope measurements, Infrared Phys. Techn., 51, 198–206, doi:10.1016/j.infrared.2007.05.006, 2008b.

Tuzson, B., Henne, S., Brunner, D., Steinbacher, M., Mohn, J., Buchmann, B., and Emmenegger, L.: Continuous isotopic composition measurements of tropospheric CO_2 at Jungfraujoch (3580 m a.s.l.), Switzerland: real-time observation of regional pollution events, Atmos. Chem. Phys., 11, 1685–1696, doi:10.5194/acp-11-1685-2011, 2011.

Uglietti, C., Leuenberger, M., and Brunner, D.: European source and sink areas of CO_2 retrieved from Lagrangian transport model interpretation of combined O_2 and CO_2 measurements at the high alpine research station Jungfraujoch, Atmos. Chem. Phys., 11, 8017–8036, doi:10.5194/acp-11-8017-2011, 2011.

van der Laan-Luijkx, I. T., van der Laan, S., Uglietti, C., Schibig, M. F., Neubert, R. E. M., Meijer, H. A. J., Brand, W. A., Jordan, A., Richter, J. M., Rothe, M., and Leuenberger, M. C.: Atmospheric CO_2, $\delta(O_2/N_2)$ and $\delta^{13}CO_2$ measurements at Jungfraujoch, Switzerland: results from a flask sampling intercomparison program, Atmos. Meas. Tech. Discuss., 5, 7293–7322, doi:10.5194/amtd-5-7293-2012, 2012.

Vogel, F. R., Huang, L., Ernst, D., Giroux, L., Racki, S., and Worthy, D. E. J.: Evaluation of a cavity ring-down spectrometer for in situ observations of $^{13}CO_2$, Atmos. Meas. Tech., 6, 301–308, doi:10.5194/amt-6-301-2013, 2013.

Vollmer, M. K., Zhou, L., Greally, B. R., Henne, S., Yao, B., Reimann, S., Stordal, F., Cunnold, D. M., Zhang, X., Maione, M., Zhang, F., Huang, J., and Simmonds, P. G.: Emissions of ozone-depleting halocarbons from China, Geophys. Res. Lett., 36, L15823, doi:10.1029/2009GL038659, 2009.

Welp, L. R., Keeling, R. F., Meijer, H. A. J., Bollenbacher, A. F., Piper, S. C., Yoshimura, K., Francey, R. J., Allison, C. E., and Wahlen, M.: Interannual variability in the oxygen isotopes of atmospheric CO_2 driven by El Nino, Nature, 477, 579–582, doi:10.1038/nature10421, 2011.

Werle, P., Mücke, R., and Slemr, F.: The limits of signal averaging in atmospheric trace-gas monitoring by tunable diode-laser absorption spectroscopy (TDLAS), Appl. Phys. B-Lasers O., 57, 131–139, 1993.

Werner, R., Rothe, M., and Brand, W.: Extraction of CO_2 from air samples for isotopic analysis and limits to ultra high precision $\delta^{18}O$ determination in CO_2 gas, Rapid Commun. Mass Sp., 15, 2152–2167, doi:10.1002/rcm.487, 2001.

Wingate, L., Ogée, J., Cuntz, M., Genty, B., Reiter, I., Seibt, U., Yakir, D., Maseyk, K., Pendall, E. G., Barbour, M. M., Mortazavi, B., Burlett, R., Peylin, P., Miller, J., Mencuccini, M., Shim, J. H., Hunt, J., and Grace, J.: The impact of soil microorganisms on the global budget of $\delta^{18}O$ in atmospheric CO_2, P. Natl. Acad. Sci., 106, 22411–22415, doi:10.1073/pnas.0905210106, 2009.

WMO: 15th WMO/IAEA Meeting of Experts on Carbon Dioxide, Other Greenhouse Gases and Related Tracers Measurement Techniques, Tech. Rep. WMO/TD-No. 1553, WMO, Geneva, 2011.

Yakir, D.: The Stable Isotopic Composition of Atmospheric CO_2, in: Treatise on Geochemistry, edited by: Holland, H. D. and Turekian, K. K., Vol. 4, 175–212, Pergamon, Oxford, doi:10.1016/B0-08-043751-6/04038-X, 2003.

Zellweger, C., Forrer, J., Hofer, P., Nyeki, S., Schwarzenbach, B., Weingartner, E., Ammann, M., and Baltensperger, U.: Partitioning of reactive nitrogen (NO_y) and dependence on meteorological conditions in the lower free troposphere, Atmos. Chem. Phys., 3, 779–796, doi:10.5194/acp-3-779-2003, 2003.